# Changes in Oceanic Carbon Storage due to Anthropogenic Carbon Input over the Past Three Decades

# Fengjue Hong<sup>1</sup>, Varvara E. Zemskova<sup>2</sup>

- <sup>1</sup>University of Waterloo, Department of Geography and Environmental Management, 200 University Ave
  W, Waterloo, ON N2L 3G1, Canada
  <sup>2</sup>University of Waterloo, Department of Applied Mathematics, 200 University Ave W, Waterloo, ON N2L
- This is a non-peer-reviewed preprint that has been submitted to Global Biogeochemical Cycles.

# Key Points:

10

11

13

14

16

- We evaluate trends in the ocean anthropogenic carbon concentrations for 1992-2022 using an ocean state estimate ECCO-Darwin model.
- Over this period, the ocean uptake of anthropogenic DIC accounts for approximately 28% of carbon emissions.
- Ocean anthropogenic carbon storage predominantly occurs within the upper ocean and has been increasing at an accelerated rate.

Corresponding author: Varvara E. Zemskova, barbara.zemskova@uwaterloo.ca

#### Abstract

18

19

20

22

23

24

25

26

27

30

31

32

33

34

35

36

37

38

40

41

42

43

45

46

47

49

50

While the ocean is known to be an important sink for anthropogenic CO<sub>2</sub> emissions, assessing trends in ocean's uptake and storage of atmospheric CO<sub>2</sub> is complicated because changes in the ocean dissolved inorganic carbon (DIC) concentrations due to natural ocean circulation patterns and flux of anthropogenic  $CO_2$  need to be disentangled. In this study, we analyze the interannual and decadal changes in the ocean anthropogenic DIC storage from 1992 to 2022 using data from the physically and biogeochemically consistent ECCO-Darwin ocean state estimate model. We use the quasi-conservative tracer C\* to represent the ocean anthropogenic DIC concentrations and offer several key extensions to previous studies: (1) a longer period of analysis (three decades), (2) analysis including the Arctic Ocean, (3) regular spatio-temporal coverage using annually-averaged data to more accurately estimate the rates of change of C\*. Over the 1992–2022 period, we estimate a total global ocean C\* increase of 60 Pg C, corresponding to about 28% of total anthropogenic CO2 emissions during this time. The general temporal trend shows a nonlinear increase with accelerating rates of anthropogenic DIC accumulation especially in the last two decades (2002–2022), though a slowdown in the increasing rates is found in some parts of the ocean, in particular in high-nutrient low-chlorophyll regions. Empirical Orthogonal Function analysis of the vertically-integrated rates of change of C\* reveals that the top three modes of interannual variability correspond to equatorial and tropical climate modes, such as El Niño Southern Oscillation, Atlantic Niño, and El Niño Modoki.

# Plain Language Summary

The ocean is known to be responsible for taking up a large portion of carbon dioxide released into the atmosphere by human activities such as burning fossil fuels. However, when considering changes in the ocean carbon concentrations, it is difficult to determine what proportion is due to natural oceanic processes versus uptake of carbon of anthropogenic origin. Here we use data from a global-ocean biogeochemistry model to separate out specifically the changes in ocean anthropogenic carbon concentrations and examine the spatial and temporal trends over the 1992–2022 time period. We find that over this 31 year period, the ocean anthropogenic carbon content has increased by approximately 28% of total anthropogenic carbon dioxide emissions. We also find that while the ocean uptake and storage of anthropogenic carbon has been increasing at an accelerated rate in many parts of the ocean, the rate of increase has slowed down in some critical ocean regions, which suggests the need for further monitoring.

#### 1 Introduction

52

53

54

55

56

57

58

61

62

63

65

69

70

71

72

73

74

75

76

77

78

80

81

82

83

85

86

87

89

90

93

94

100

101

102

103

The ocean plays a critical role in the Earth system; it stores, absorbs, releases, and exchanges carbon from the atmosphere. It is the second largest carbon reservoir, which stores approximately 60 times as much carbon as the atmosphere, surpassed only by the solid Earth, mostly in limestone and shale rocks which stores roughly 100,000 times more carbon than the atmosphere (DeVries, 2022). Since the Industrial Revolution, human activities have led to the continuous emissions of large amounts of carbon dioxide (IPCC, 2023). The large carbon emissions in the atmosphere not only changed the composition of the atmosphere, but also significantly aggravated the instability of the ocean's carbon absorption mechanism (IPCC, 2023). This has led to an imbalance in the carbon cycle that has long maintained the stability of the Earth's climate, such as risk to the ecosystems and threats to human development (Trebilco et al., 2022). Specifically, the large amount of carbon emissions has triggered a series of environmental crises such as global warming, frequent extreme weather, and rising sea levels (United Nations Development Programme (UNDP), 2023). Low-income regions and island countries on the socioeconomic margins are particularly vulnerable to these changes (Luetz & Merson, 2020; Chin-Yee, 2019). Rising ocean temperatures and acidification affect the stability of fishery ecology and food chains, exacerbating the survival pressure on groups that rely on marine resources for their livelihoods (Trebilco et al., 2022).

Therefore, there is an imminent need to understand the temporal trends in ocean carbon sink to assess the ocean's potential to take up more carbon dioxide from the atmosphere. In response to the increase in atmospheric carbon and changes to the Earth's carbon cycle, numerous studies investigated the ocean carbon flux and the dissolved inorganic carbon (DIC) budget. For example, recent studies on ocean carbon storage at the decadal scales have shown that while from the 1990s to early 2000s, the global ocean carbon sink was decreasing, in the 2000s and 2010s, the ocean carbon sink has strengthened (Landschützer et al., 2015; DeVries et al., 2019; Zemskova et al., 2022). However, as ocean DIC measurements are sparse (L. Talley et al., 2016), there have been many different methodologies employed to attempt to capture the spatial and temporal (both short-term such as seasonal cycles, and long-term, such as interannual and decadal scales) patterns.

The DIC budget changes are controlled not only at the ocean surface but also within the ocean interior by several processes: physical processes, biogeochemical processes, thermodynamic effects, and anthropogenic impacts (Sarmiento & Gruber, 2006; Carroll et al., 2022). Physical processes include advection, diffusion and mixing, and air-sea CO<sub>2</sub> flux. Advection is characterized by the large-scale ocean circulation transports water masses with varying DIC concentrations, whereas diffusion and mixing act on small spatiotemporal scales primarily redistributing DIC across depth layers, shaping vertical DIC gradients. Air-sea CO<sub>2</sub> flux is the exchange of CO<sub>2</sub> between sea surface and the atmosphere, which directly affects the surface DIC concentration. Anthropogenic emissions impact increase the total atmospheric CO<sub>2</sub>, which gradually enters the ocean through the air-sea CO<sub>2</sub> flux, causing the rise in surface DIC concentrations over time. Biogeochemical processes include changes to the ocean DIC pool through net community production (i.e., incorporation of DIC into the organic matter pool through photosynthesis) and remineralization (i.e., decomposition of organic matter back into inorganic components). Thermodynamic effects are due to changes in ocean temperature; for example, the increasing temperature in ocean decreases the solubility of CO<sub>2</sub> in seawater, thereby influencing the equilibrium distribution of DIC, especially at the surface. As such, both the natural and anthropogenic processes can change the DIC in ocean, and it is necessary to separate the effects of the two on the ocean DIC spatio-temporal trends.

Many studies have aimed to monitor the changes in ocean carbon sink by estimating air-sea carbon fluxes at the ocean surface (e.g., Fay & McKinley, 2013; Gregor & Gruber, 2020; Rödenbeck et al., 2015, 2021). For example, Landschützer et al. (2015) ap-

plied a neural network approach to interpolate the sparse and spatio-temporally heterogeneous observations of surface partial pressure of  $\rm CO_2$  (pCO<sub>2</sub>) to study the Southern Ocean carbon sink. Bushinsky et al. (2019) compared the different interpolation strategies assessing how data from biogeochemical Argo floats can augment the shipboard observations, which are in particular scarce in the winter in the Southern Ocean. In another study, Mayot et al. (2024) used a hybrid approach combining the physical and biogeochemical coupled model NEMO-PlankTOM12.1 and observed SOCAT fCO<sub>2</sub> (fugacity of carbon dioxide) data at the surface to improve the model estimates, specifically to constrain the trend of the ocean carbon sink from 2000 to 2022. The study showed this method can help minimize the differences between process-based numerical models and observations of estimated global carbon budget over this period.

105

106

107

109

110

111

112

113

114

115

116

117

118

119

121

122

123

124

125

126

127

129

130

131

132

133

134

135

136

137

138

139

141

142

143

144

145

146

149

150

151

152

153

154

156

157

158

In recent years, there also have been efforts to understand the variability of DIC within the ocean interior through climatological averages (e.g., Bronselaer et al., 2020; Lauvset et al., 2022), coupled ocean circulation models (e.g., Verdy & Mazloff, 2017; Carroll et al., 2020), and machine-learning methods (e.g., Broullón et al., 2020; Keppler et al., 2020; Zemskova et al., 2022; Keppler et al., 2023). However, in addition to differences, both in total magnitude and regionally, across methods in estimating ocean carbon uptake (DeVries et al., 2023; Gray, 2024), these datasets do not provide the breakdown between the natural and anthropogenic-driven changes in the ocean DIC pool. One of the methods to estimate the natural DIC signal uses the organic matter remineralization stochiometric ratios relating DIC to either dissolved oxygen concentrations (Gruber et al., 1996) or dissolved nitrate, and phoshate concentrations (Gruber & Sarmiento, 2002). This method has been successfully implemented to provide estimates in changes of DIC of natural and anthropogenic origin along certain repeated hydrographic transects (Sabine et al., 1999; Wanninkhof et al., 2010; Carter et al., 2019) and globally (Gruber et al., 2019; Mayot et al., 2024). However, because this methodology relies on the readily available data for other biogeochemical variables (e.g., oxygen, nitrate, or phosphate) in the ocean interior, these studies have only been able to provide estimates for inter-decadal changes in the natural and anthropogenic DIC inventories, which do not account for inter-annual variability and longer-term climatological cycles such as El Niño Southern Oscillation (ENSO) that have been shown to play an important role in distribution of ocean DIC (Carroll et al., 2022; Keppler et al., 2023; DeVries et al., 2023).

To address this limitation of the previous studies, we apply the methodology of Gruber and Sarmiento (2002) to the output of the ECCO-Darwin model (Carroll et al., 2020), which provides three-dimensional data for biogeochemical variables on regular spatiotemporal intervals, to estimate annual changes in the global ocean storage of anthropogenic DIC over the 1992-2022 period. The ECCO-Darwin model is a global ocean biogeochemistry model that couples the Estimating the Circulation and Climate of the Ocean (ECCO) model for physical processes in the ocean and an ecosystem model developed by the Massachusetts Institute of Technology Darwin Project. One of its major advantages is that it produces continuous, observation-constrained (by data from GLODAPv2 (Lauvset et al., 2022) and other observational databases) outputs for biogeochemical variables (e.g., DIC, nitrate, phosphate, alkalinity, and dissolved oxygen) and physical variables (e.g., temperature, salinity, flow velocity) across seasonal to multidecadal timescales (Carroll et al., 2020). Because ECCO-Darwin produces three-dimensional fields of the biogeochemical variables on across a set spatial grid at regular temporal intervals with full spatial and temporal coverage regardless of observation density, it allows us to calculate the natural and anthropogenic changes in DIC at every model grid point and at every available timestep. Specifically, in this study, we report annual changes, ignoring smaller scale (e.g., seasonal) variations, on a  $1^{\circ} \times 1^{\circ}$  horizontal grid from the surface to the ocean bottom to gain a more comprehensive understanding of spatio-temporal trends of the ocean DIC changes decomposed into the natural and anthropogenic components. We acknowledge that because we are using model-based data as input, our results are subject to any biases that originate from the model configuration, for example, from the

parameterization of unresolved small-scale processes or simplification of the biogeochemical cycles. However, with these caveats, this paper provides another set of independent estimates of the natural and anthropogenic ocean DIC changes to better constrain the estimates of ocean carbon storage trends in conjunction with previous studies.

## 2 Data and Methods

159

160

161

163

164

165

166

167

168

169

170

172

173

174

175

176

177

178

180

181

182

183

186

187

188

189

190

193

194

195

197

198

201

202

203

206

207

## 2.1 Overview of the Approach

This study uses the carbon tracer as a proxy for anthropogenic carbon  $C^*$  developed by Gruber et al. (1996), which is one of the standard framework for estimating anthropogenic carbon in the ocean. It also adopts the framework of  $\Delta C^*$  to quantify the temporal anthropogenic carbon storage changes, following Gruber et al. (2019) and Müller et al. (2023). Unlike their observation-based approach that relies on regression-based interpolation of the spatio-temporally sparse cruise data, this study applies a simplified version of the method using annual data on a regular grid from the ECCO-Darwin model. Furthermore, the spatio-temporally continuous nature of the data allows us to directly calculate temporal trends of  $\Delta C^*$  without the need for reference year adjustment unlike Gruber et al. (2019) and Müller et al. (2023). In a similar approach to Müller et al. (2023), the oceans are separated into five basins that are then divided based on neutral density ranges, such that there are 45 regions in total. The study uses the data from the ECCO-Darwin model available from 1992 to 2022 to calculate  $C^*$  and the temporal changes in  $C^*$  over certain time periods (both annual and decadal) across the different ocean regions.

#### 2.2 Data Used

The estimates in this study are based on the data from the ECCO-Darwin model, which is a global ocean biogeochemistry model that combines the global ocean circulation model (physical module) from the Estimating the Circulation and Climate of the Ocean (ECCO) consortium and an ecosystem model (biogeochemical module) developed by the Massachusetts Institute of Technology Darwin Project (Carroll et al., 2020). The ECCO-Darwin ocean state estimate combines a general circulation model with a biogeochemical model through a four-dimensional variational (4D-Var) adjoint assimilation framework (Carroll et al., 2020). In the physical module, the MITgcm ocean circulation model is constrained by a wide range of observational datasets, including satellite altimetry, sea surface temperature, sea ice concentration, and in situ hydrographic profiles from Argo floats, ship-based CTD casts, and moorings. The adjoint method iteratively adjusts model control variables (e.g., surface forcing, initial conditions, and mixing parameters) to minimize the misfit between model output and observations over the full assimilation window. The coupled biogeochemical module (Darwin Project) simulates multiple phytoplankton and zooplankton functional types with variable elemental stoichiometry, allowing for competition and adaptation to changing environmental conditions (Carroll et al., 2020, 2022). The carbon cycle component explicitly represents DIC, alkalinity, nutrients (phosphate, nitrate, silicate), dissolved oxygen, and dissolved organic matter pools (Carroll et al., 2020, 2022). Air–sea CO<sub>2</sub> exchange, remineralization, and biological export production are all resolved within the model framework, providing physically and biogeochemically consistent estimates of the evolving ocean carbon system (Carroll et al., 2020, 2022).

The ECCO-Darwin model is run on a LLC270 (Lat-Lon-Cap 270) grid, which organizes the global ocean into 13 spatial tiles, each with  $270\times270$  horizontal grid points (Carroll et al., 2020). For the ease of visualization, we converted the data onto a regular latitude-longitude grid with 1° horizontal resolution. This resolution was chosen to be consistent with other major ocean biogeochemical datasets, e.g., the World Ocean Atlas (WOA). However, any other horizontal spacing larger than  $1/3^\circ$  degree (the largest

horizontal spacing in the native LLC270 grid) could have been chosen. As the focus of this study is on the annual-scale variability of anthropogenic carbon storage in the oceans, all variables were aggregated into annual means by averaging over the 12 monthly values for each year from 1992 to 2022. No masking and further data cleaning was required in this step as the ECCO-Darwin model provides fully gridded and physically consistent data without missing values over the ocean.

Compared with the real-world observations, the modeled data has a high similarity with observed data in data-rich areas, particularly for temperature, salinity, dissolved oxygen, and alkalinity, as evaluated against datasets such as the World Ocean Atlas (WOA), Argo, and GLODAPv2 (Carroll et al., 2022). For example, in the ECCO-Darwin state estimate, the optimized simulation reduced the total model—data misfit to 31.9% of the first-guess simulation from Brix et al. (2015), with particularly strong improvements for hydrographic and biogeochemical variables such as temperature, salinity, dissolved oxygen, and DIC. These improvements were evaluated against WOA and Argo observations (Carroll et al., 2020), and, in the extended 1992–2018 version, also against GLODAPv2 biogeochemical data (Carroll et al., 2022). For further details and validations of the model, the readers should refer to Carroll et al. (2020) and Carroll et al. (2022).

# 2.3 $C^*$ calculation

As the ocean total DIC is a combination of naturally-produced carbon due to oceanic biogeochemical activity and anthropogenic carbon absorbed from the atmosphere, the method proposed by Gruber et al. (1996) can separate the two by isolating a tracer  $C^*$  which represents the anthropogenic carbon. The  $C^*$  tracer is computed as:

$$C^* = DIC - r_{C:P} \cdot PO_4 - 0.5 \cdot (Alk + r_{N:P} \cdot PO_4)$$
(1)

where PO<sub>4</sub> (phosphate) and ALK (alkalinity) are used to approximate the natural DIC component based on canonical Redfield stoichiometric ratios, with  $r_{C:P} = 117$  and  $r_{N:P} =$ 16. The resulting residual represents the anthropogenic fraction of DIC, as it cannot be explained by natural biological cycling (Clement & Gruber, 2018). The variables of PO<sub>4</sub>, ALK and DIC are retrieved from ECCO-Darwin model output, with a valid period of 1992 to 2022. The Redfield stoichiometric ratios is extracted from Anderson and Sarmiento (1994). Here, we follow the same assumption as previous studies that estimated changes in ocean anthropogenic DIC (Clement & Gruber, 2018; Gruber et al., 2019; Müller et al., 2023) that the variations in the Redfield ratio are predominantly spatial (Martiny et al., 2013; Liefer et al., 2024; Seelen et al., 2025) and will not affect temporal trends in  $C^*$  at any given location. However, it is important to note that recent studies found temporal shifts in stoichiometric ratios to be important (Hutchins & Tagliabue, 2024; Liu et al., 2025), which may need to be incorporated into the calculation of  $C^*$  in future studies as an uncertainty parameter. Also, as noted in Clement and Gruber (2018),  $C^*$ contains a generally much smaller component of the natural air-sea CO<sub>2</sub> exchange, but predominantly  $C^*$  reflects the uptake of anthropogenic  $CO_2$ .

In order to estimate the changes in oceanic DIC from the uptake of anthropogenic carbon, we compute  $\Delta C^*$  as in previous studies (Gruber et al., 2019; Müller et al., 2023). In our case, we have annually-averaged data, so we can compute the year-to-year changes between year  $t_2$  and year  $t_1$  at each grid point as:

$$\Delta C^*(t_1, t_2) = C^*(t_2) - C^*(t_1) \tag{2}$$

In addition to the annual changes in  $C^*$ , we also compute decadal trends to compare with those based on interpolated observational data presented in previous studies (Gruber et al., 2019; Müller et al., 2023). For our data, to quantify decadal changes in anthropogenic carbon storage, linear regression is applied to annual  $C^*$  values at each grid cell over selected time periods. We compute decadal changes over three decadal periods: 1993 –

, 2003-2012, and 2013-2022 corresponding to the total span of the ECCO-Darwin model dataset.

## 2.4 Ocean Basin Mask and Regional Classification

While all of the anthropogenic DIC trend analysis is conducted at each latitude-longitude-depth grid point separately, this study also provides analysis of the anthropogenic DIC trends aggregated over certain ocean regions. First, the global ocean is divided horizontally into five basins based on the basin mask provided by the WOA database (Locarnini et al., 2023): Atlantic, Pacific, Indian, Southern, and Arctic. This division is similar to the one used for analysis in Müller et al. (2023); however, this previous study did not provide estimates for the Arctic Ocean due to the lack of observational data. We consider the Southern Ocean separately, as it has been noted as an important region for the DIC budget (e.g., Landschützer et al., 2015; Zemskova et al., 2022) and was similarly considered separately in other studies of anthropogenic carbon (e.g., Keppler et al., 2023).

We also divide the ocean vertically; however, instead of the depth levels, we use ranges of neutral density  $\gamma$  (Jackett & McDougall, 1997). This is a convenient coordinate system for ocean's isopycnals (layers of constant density) adjusted for reference pressure levels (which increase with depth). The flow and the distribution of tracers (both active tracers like temperature and passive tracers like DIC and other chemicals) primarily follows isopycnals (L. D. Talley, 2013). While the isopycnals are horizontal and align with the depth layers throughout most of the ocean, they slant towards the surface in the North Atlantic and the Southern Oceans. Therefore, it is better to divide the dynamical regions of the ocean based on neutral density rather than depth. As neutral density depends on the in-situ temperature and salinity, we used values from the WOA climatological mean (Locarnini et al., 2023) over the 1991 – 2020 time period, which most closely matches the time period for the ECCO-Darwin dataset. Neutral densities were calculated using the Gibbs-Seawater (GSW) Oceanographic Toolbox (McDougall & Barker, 2017).

The neutral density ranges were taken from Müller et al. (2023) with upper bound cutoff values of

$$\gamma = [26.00, 26.50, 26.75, 27.00, 27.25, 27.50, 27.75, 
27.85, 27.95, 28.05, 28.10, 28.15, 28.20, 30] \text{ kg/m}^3.$$
(3)

The GSW function for computing neutral densities does not cover the Arctic Ocean, so we consider it as one region without any further vertical divisions. The other four ocean basins are further divided into regions based on neutral density values. We adjust the neutral density cutoffs such that at any given timestep, there are at least 2000 grid points within a region to ensure that there are enough points for the aggregate analysis. This yields 11 regions within the Southern Ocean basin with neutral density cutoffs of

$$\gamma = [27, 27.25, 27.50, 27.75, 27.85, 27.95, 28.05, 28.10, 28.15, 28.20, 30] \text{ kg/m}^3$$

and 11 regions within each of the Atlantic, Pacific, and Indian Ocean basins with neutral density cutoffs of

```
\gamma = [26, 26.50, 26.75, 27, 27.25, 27.50, 27.75, 27.85, 27.95, 28.05, 30] \text{ kg/m}^3.
```

A range of  $\gamma < 26~{\rm kg/m^3}$  corresponds to the neutral density layer located between the surface and 150 m at the subtropical latitudes. As a result, the five ocean basins are separated into 45 regions in total.

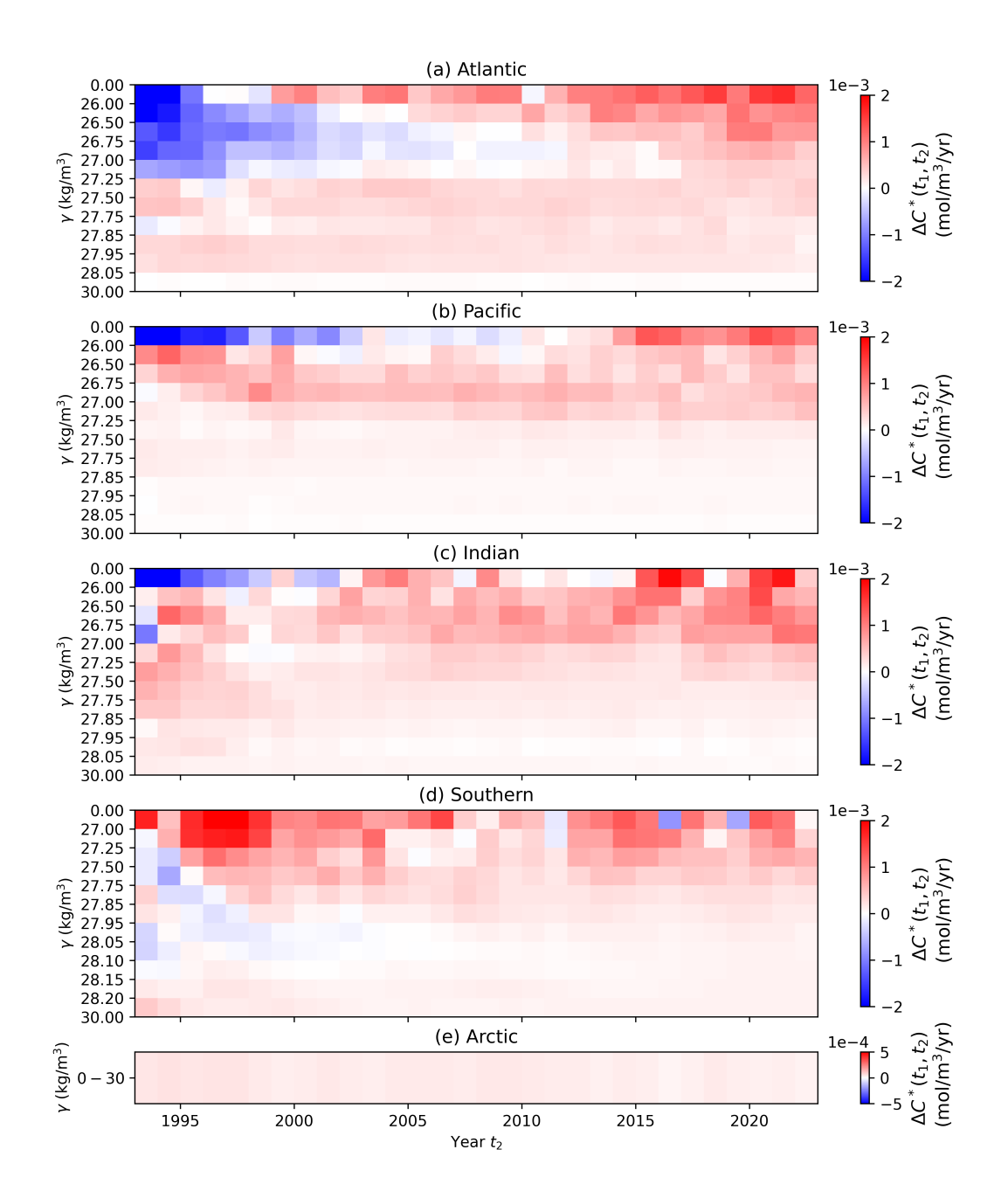


Figure 1. Year-to-year changes in  $C^*$  ( $\Delta C^*(t_1,t_2)$ ) from 1992 to 2022 across five ocean basins: (a) Atlantic, (b) Pacific, (c) Indian, (d) Southern, and (e) Arctic oceans. The four ocean basins except the Arctic are further subdivided into neutral density layers (see § 2.4 for details). Note the differences in the colorbar for (e). The red colors represent increases ( $\Delta C^* > 0$ ), and the blue colors represent decreases ( $\Delta C^* < 0$ ) in the ocean anthropogenic DIC concentrations averaged over the particular ocean subregion.

# 3 Results

## 3.1 Interannual variability of $C^*$

First, we examine shorter-term change in the oceanic storage of anthropogenic carbon  $(C^*)$ , namely a year-to-year change. Figure 1 shows ocean  $\Delta C^*(t_1, t_2)$ , where  $t_1$  and  $t_2$  are two consecutive years, in different ocean basins over the 1992–2022 period with detailed information over different neutral density ranges (proxy for depth layers), i.e., for the 45 different ocean basins described in § 2.4. Overall, we find a predominantly positive trend in all five ocean basins for the year-to-year changes of  $\Delta C^*$  ( $\Delta C^* > 0$ ), indicating a general increase in the ocean storage of anthropogenic carbon over the analyzed period. In particular, after 2012,  $\Delta C^* > 0$  for almost all  $\gamma$  layers. Unlike other ocean basins that have intermittent periods of decreasing  $C^*$  trends, the Arctic Ocean exhibits increasing ocean DIC trends over the entire time range. Overall, the rates of largest magnitude are in shallower (less dense) layers, whereas we find mostly weakly positive trends in the denser  $\gamma$  layers, suggesting less anthropogenic DIC accumulation in the deeper ocean. Figure 1 exhibits intermittency in the sign and magnitude of  $\Delta C^*$ , which suggests that interannual variability in the ocean DIC is important when considering changes in the ocean's ability to take up more atmospheric carbon.

The  $\Delta C^*$  timeseries in Figure 1 also reveals connectivity of certain ocean basins through global ocean circulation. Specifically, we find negative ocean DIC trends propagating from near the surface (lower values of  $\gamma$ ) into the ocean interior (larger values of  $\gamma$ ) in the Atlantic over the 1992–2005 period (Fig. 1(a)). These  $\gamma$  layers are in the range of Mode Water and Intermediate Water, suggesting a decrease in the anthropogenic DIC uptake and delivery into the ocean interior in the North Atlantic, potentially due to weakening Atlantic Meridional Overturning Circulation (AMOC) (Pérez et al., 2013; Gruber et al., 2019). With a slight temporal delay, we find decreasing trends within the Antarctic Intermediate Water (AAIW,  $\gamma \in [27, 27.5] \text{ kg/m}^3$ ) that are then transported to denser Circumpolar Deep Water (CDW,  $\gamma \in [27.5, 28] \text{ kg/m}^3$ ) ranges, most likely within the upwelling region in the Southern Ocean that is part of the AMOC cell (Fig. 1(d)). Analyzing the annual rather than decadal changes in  $C^*$  over the different  $\gamma$  layers allows us to better track and attribute trends to the ocean circulation patterns.

Interestingly, we find that over the similar period (1995–1999),  $C^*$  in the lighter  $\gamma$  ranges in the Southern Ocean ( $\gamma \leq 27.5 \text{ kg/m}^3$ ) was increasing at a high rate. These trends, indicative of possible DIC saturation in near-surface ocean layers, align with the previous findings of faster increase in surface ocean  $\text{CO}_2$  compared to the atmosphere and thus a decreasing ocean DIC sink in the 1990s by Landschützer et al. (2015). While  $\Delta C^*$  is still positive in those  $\gamma$  layers in the 2000, the magnitude is lower consistent with the reinvigoration of the Southern Ocean carbon sink (Landschützer et al., 2015). These trends in the 1990s also suggest a compensation by the Southern Ocean to take up additional anthropogenic carbon during the period of reduction of such uptake in the North Atlantic, also noted in previous studies (Gruber et al., 2019; Müller et al., 2023). We do not find such compensation in later periods as  $\Delta C^*$  is almost uniformly positive; however, it is possible that this is part of a longer-term ocean circulation patterns that are not fully captured in the 30 years analyzed here.

# 3.2 Decadal variability of $C^*$

In this section, we will examine the decadal changes in ocean anthropogenic DIC concentrations for three decades: 1993–2002, 2003–2012, and 2013–2022. Following Müller et al. (2023), we examine the spatial patterns in two ways. First, in § 3.2.1 we consider vertically-integrated  $\Delta C^*$  over the entire water column from the local maximum depth to the surface, which we will denote as  $\widehat{\Delta C}^*(x,y)$  as a function of latitude x and longitude y. Next, in § 3.2.2 we explore zonally-integrated  $\Delta C^*$  for each of the five (At-

lantic, Pacific, Indian, Southern, and Arctic) ocean basins, denoted as  $\widetilde{\Delta C}^*(x,z)$  at each latitude x and depth z.

We also compare these spatial patterns of  $\widehat{\Delta C}^*(x,y)$  and  $\widehat{\Delta C}^*(x,z)$  with those in Müller et al. (2023). One of the key differences in methodology is that Müller et al. (2023) had to consider an aggregate of available observations over each of the three time periods (1989 – 1999, 2000 – 2009, and 2010 – 2020) and calculate  $C^*$  referenced to a particular year for each time period (1994, 2004, and 2014, respectively). The change in ocean anthropogenic DIC, i.e.,  $\Delta C^*$ , was then estimated as the change between the reference years (1994–2004 and 2004–2014). In contrast, because we use ECCO-Darwin model data that is regularly gridded in space and time, we are able to calculate  $\Delta C^*(x,y,z)$  for each ocean grid cell more directly as a linear regression over each decade that we consider (1993 – 2002, 2003 – 2012, and 2013 – 2022). We also considered the same time periods as Müller et al. (2023) (1994–2004 and 2004–2014) for our dataset (not shown) and found them to have similar patterns to the 1993 – 2002 and 2003 – 2012 time periods, so for brevity, we will only present and discuss the 1993–2002, 2003–2012, and 2013 – 2022 periods.

# 3.2.1 Vertically-averaged decadal changes in $C^*$

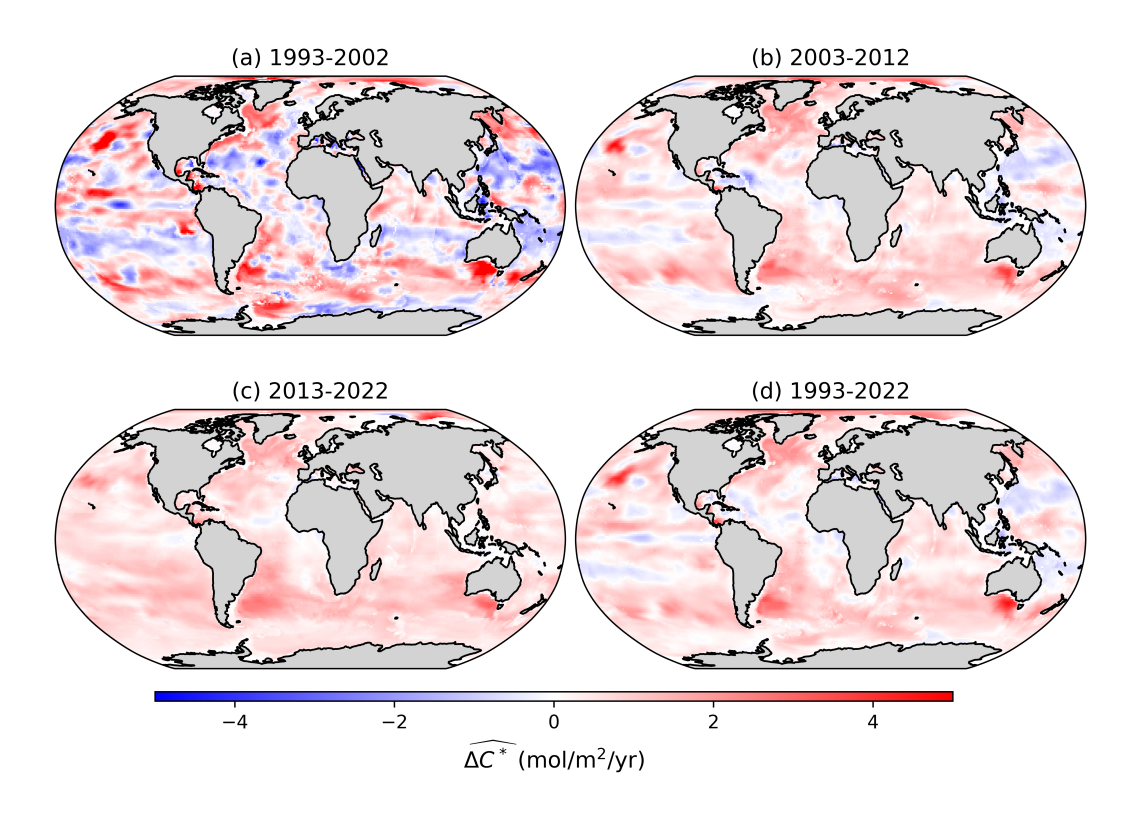


Figure 2. Vertically-integrated decadal changes in ocean anthropogenic carbon inventory  $\widehat{\Delta C^*}$  for three decades separately (a) 1993 - 2002, (b) 2003 - 2012, (c) 2013 - 2022 and the full period (d) 1993 - 2022. Positive (negative) values correspond to overall increase (decrease) in ocean anthropogenic carbon concentrations. Land is shaded in grey.

All decades show widespread increasing trends in ocean anthropogenic DIC concentration  $(\widehat{\Delta C^*}(x,y)>0)$  in Figure 2(a-c)). There are several areas that stand out with larger increasing rates, many within the Eastern Boundary Current regions. In the Atlantic region, the large increasing trends  $(\widehat{\Delta C^*}\approx 18.0 \text{ mol m}^{-2} \text{ dec}^{-1})$  appear over

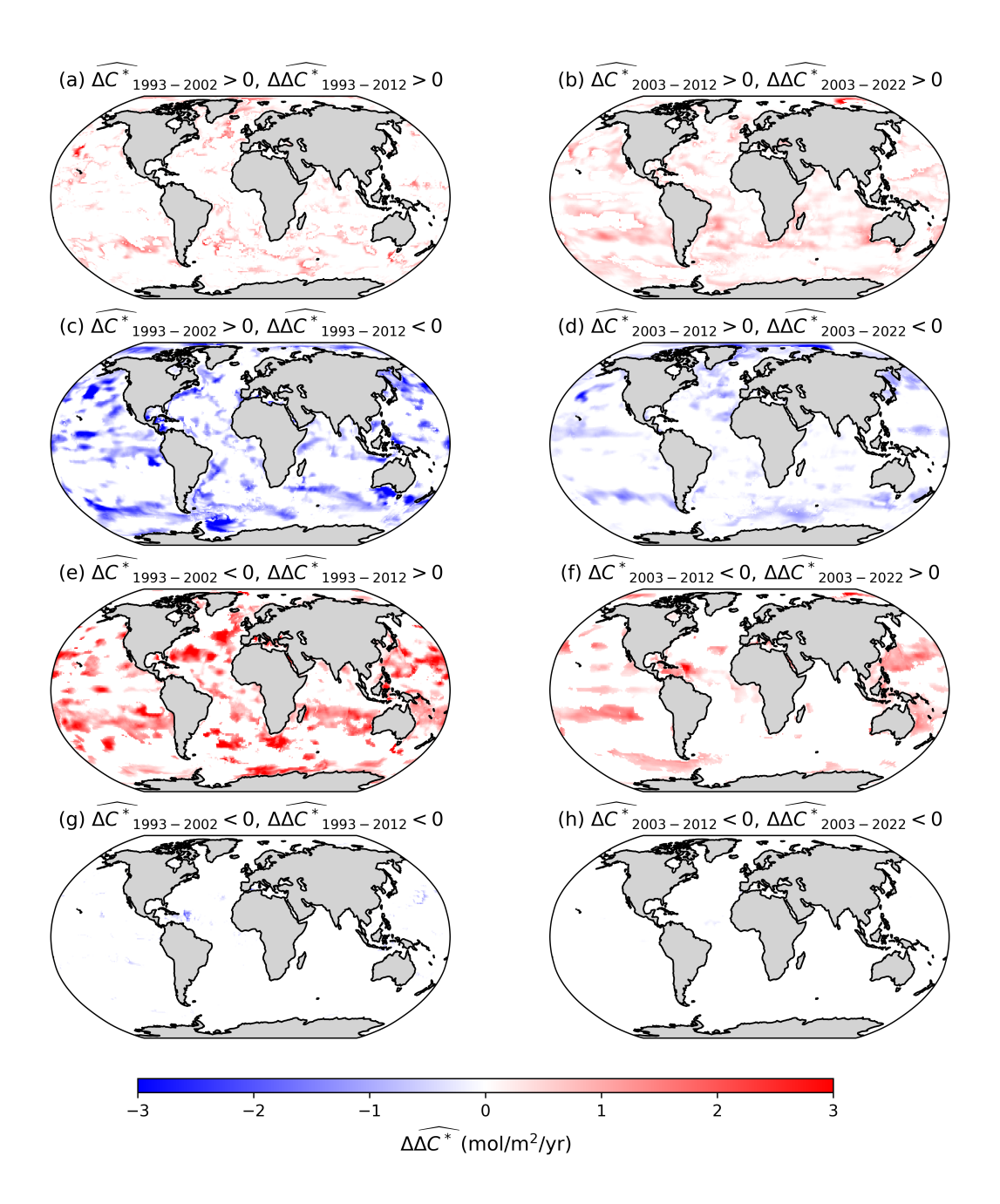


Figure 3. Comparison of decadal differences in the rates of change anthropogenic carbon storage. The maps show the decadal differences in the vertically-integrated ocean anthropogenic carbon inventory  $\widehat{\Delta C^*}$  ( $\Delta \widehat{\Delta C^*}$ ), that is difference between: (a, c, e, g) 2003–2012 and 1993–2002, and (b, d, f, h) 2013–2022 and 2003–2012. Subplots are separated by the sign of  $\Delta \widehat{\Delta C^*}$  and  $\widehat{\Delta C^*}$  of the first period: (a, b)  $\Delta \widehat{\Delta C^*}$  > 0,  $\widehat{\Delta C^*}$  > 0, (c, d)  $\Delta \widehat{\Delta C^*}$  < 0,  $\widehat{\Delta C^*}$  > 0, (e, f)  $\Delta \widehat{\Delta C^*}$  > 0,  $\widehat{\Delta C^*}$  < 0, and (g, h)  $\Delta \widehat{\Delta C^*}$  < 0,  $\widehat{\Delta C^*}$  < 0. The color in each subplot corresponds to the value of  $\Delta \widehat{\Delta C^*}$ . Land is shaded in grey.

366

367

370

371

372

373

374

377

378

381

382

384

385

388

389

390

391

392

393

396

397

398

401

402

403

404

405

407

408

409

410

411

412

the North Atlantic along the Gulf Stream and between  $45-65^{\circ}$ N, and along the east coast of South America within the Brazil Current region  $(20-50^{\circ}\text{S})$ . In the Pacific Ocean, we find the large increasing rates in the northern part along the Kuroshio and in the equatorial region  $(5-10^{\circ}\text{N})$  along the equatorial currents. In the Indian ocean, the region south of Australia  $(300-330^{\circ}\text{E longitude}, \text{ around } 30-50^{\circ}\text{S})$  has large  $\widehat{\Delta C}^*$  values. The temporal trends in ocean carbon storage in the Southern Ocean are predominantly positive, though not exceeding 20 mol m<sup>-2</sup> dec<sup>-1</sup>, whereas in many parts of the Arctic  $(50-320^{\circ}\text{E band})$ ,  $\widehat{\Delta C}^* \geq 20$  mol m<sup>-2</sup> dec<sup>-1</sup>. Overall, we find these regions with larger positive values of  $\widehat{\Delta C}^*$  to align with those identified by Gruber et al. (2019) and Müller et al. (2023), though the magnitude of our values is larger by up to a factor of two.

The decreasing trends are predominantly noticeable in the 1993 - 2002 time period, and the area with decreasing trends diminishes with time, such that  $\Delta C^*(x,y) >$ 0 almost everywhere in the last decade (2013 - 2022). Over the 1993 - 2002 time period, regions with  $\Delta C^* < 0$  are predominantly found in the centers of subtropical gyres within the  $10-30^{\circ}$  latitudinal bands in both Northern and Southern Hemispheres throughout the North Atlantic, South Pacific, South Indian, and western part of the North Pacific Ocean regions. Interestingly, these latitudinal bands with  $\Delta C^* < 0$  are not as coherent in the Southern Atlantic Ocean, where there is a strong signal of increasing ocean anthropogenic DIC concentrations off the coast of South America. Regions with large magnitude of decreasing anthropogenic DIC trends in the ocean were not previously reported in Gruber et al. (2019) and Müller et al. (2023). It is possible that they are in part an artifact of large negative  $\Delta C^*$  during the ECCO-Darwin model spin-up period in 1992–1994 as discussed in § 3.1 (see Fig. 1). However, observational data in the 1990s was not spatio-temporally well-distributed. For example, most of observations used for the interpolation for the 1989 - 1999 time period in the Indian Ocean was from 1995and in the North Atlantic was from 1997 with generally fewer data points available prior to 1994 (Gruber et al., 2019; Müller et al., 2023). The shipboard DIC measurements used in these previous studies were also predominantly taken during the warmer months (late spring, summer, early fall) (Keppler et al., 2020). Therefore, it is possible that the previous studies were not able to accurately capture temporal variability of ocean DIC due to observational biases and data sparsity, and thus not able to capture  $\Delta C^* < 0$  in the subtropical regions that we find here.

We also find that in the Pacific and Indian Ocean sectors (150–360°E longitude) of the Southern Ocean near Antarctica ( $\approx 70^{\circ}\text{S}$ ), there is a latitudinal band with a decreasing trend in anthropogenic carbon storage (approximately  $-15 \text{ mol m}^{-2} \text{ dec}^{-1}$ ). This, overall, agrees with the regions of decreasing ocean DIC concentrations below 500 m depth in the Southern Ocean in 1993–1993 found by Zemskova et al. (2022). This finding also agrees with Gruber et al. (2019), who found lower than expected accumulation of ocean anthropogenic DIC in this region, also predominantly within the AAIW and CDW neutral density ranges (see Figure 1(d)), and attributed it to the ocean circulation changes due to the strengthening of the Westerlies.

To provide a more quantitative comparison in the changes in  $\widehat{\Delta C}^*$  between decades, we also calculate the differences between the decadal trends in  $C^*$  as

$$\Delta \widehat{\Delta C}^*(x,y)_{1993-2012} = \widehat{\Delta C}^*(x,y)_{2003-2012} - \widehat{\Delta C}^*(x,y)_{1993-2002}$$

$$\Delta \widehat{\Delta C}^*(x,y)_{2003-2022} = \widehat{\Delta C}^*(x,y)_{2013-2022} - \widehat{\Delta C}^*(x,y)_{2003-2012}.$$
(4)

This is essentially a second-order derivative of  $C^*$  with time. We can divide the temporal patterns into four categories:

1.  $\Delta \widehat{\Delta C}^* > 0$  and  $\widehat{\Delta C}^* > 0$  for the first decadal period indicating an acceleration in the increasing rates of ocean carbon storage (Fig. 3(a,b));

2.  $\Delta \widehat{\Delta C^*} < 0$  and  $\widehat{\Delta C^*} > 0$  for the first decadal period indicating a deceleration in the increasing rates or possibly a shift to decreasing rates of ocean carbon storage (Fig. 3(c,d));

413

414

415

416

417

419

421

422

423

427

428

429

431

432

433

434

435

437

438

439

442

443

444

445

448

449

451

452

454

455

457

458

460

461

462

- 3.  $\Delta \hat{\Delta} \hat{C}^* > 0$  and  $\hat{\Delta} \hat{C}^* < 0$  for the first decadal period indicating a deceleration in the decreasing rates or possibly a shift to increasing of ocean carbon storage (Fig. 3(e,f));
- 4.  $\Delta \widehat{\Delta C^*} < 0$  and  $\widehat{\Delta C^*} < 0$  for the first decadal period indicating an acceleration in the decreasing rates of ocean carbon storage (Fig. 3(g,h)).

Considering the decadal shift from the 1990s to the 2000s ( $\Delta \widehat{\Delta C}^*(x,y)_{1993-2012}$ ), we observe a pattern of compensation in ocean anthropogenic DIC uptake. Specifically, slowdown in the increasing rates of  $C^*$  (category 2, Fig. 3(c)) is found along the Eastern Boundary Currents (e.g., the Gulf Stream, Kuroshio, and Brazil Current), patch south of Australia, and many parts of the Antarctic Circumpolar Current. In contrast, within the subtropical gyres and near Antarctica in the Pacific and Indian sectors of the Southern Ocean where ocean carbon storage has been decreasing in the 1990s, there has been possibly a shift to taking up more DIC with a potential switch from negative to positive  $\widehat{\Delta C}^*$  (category 3, Fig. 3(e)).

Going from the 2000s to 2010s ( $\Delta \widehat{\Delta C}^*(x,y)_{2003-2022}$ ), data points that fall into category 1, i.e., with accelerating increasing rates of  $C^*$ , are more wide-spread (Fig. 3(b)). This suggests the reinvigoration of ocean carbon sink and generally more accelerated uptake of anthropogenic DIC by the ocean over the last two decades. Spatial patterns for regions in categories 2 (Fig. 3(d)) and 3 (Fig. 3(f)) have similar patterns to the distribution of  $\Delta \widehat{\Delta C}^*(x,y)_{1993-2012}$ , but the magnitude and area covered by regions that fall into these categories is smaller for the 2003 – 2022 period.

Finally, we acknowledge the temporal division of the data into decades is somewhat arbitrary based on the length of the available data and does not necessarily correspond to any particular natural ocean decadal cycles. Therefore, we show the total linear trend in vertically-integrated ocean storage of anthropogenic carbon from 1992 to 2022 in Figure 2(d). Spatial distribution of significantly increasing and decreasing trends are similar to those in the decade 2003-2012 (see Fig. 2(b)).

## 3.2.2 Zonally-averaged decadal changes in $C^*$

In this section, we will examine the changes in the vertical distribution of ocean anthropogenic DIC by zonally integrating  $\Delta C^*$  within each ocean basin. Figure 4 shows the zonally-averaged  $\Delta C^*$  (denoted as  $\Delta C^*$ ) across latitude and depth for each major ocean basin over the period 1992–2022. These trends highlight the meridional and vertical patterns of  $C^*$  accumulation. The rate of change of  $C^*$  is predominantly positive in all basins with a few notable areas of decreasing ocean anthropogenic DIC ( $\Delta C^*$  < 0). These regions are predominantly in the centers of subtropical gyres in the upper ( $\approx$ 500 m) Pacific and Indian Oceans and the subsurface Atlantic Ocean. Considering the breakdown of  $\Delta C^*$  into decades, these decreasing  $C^*$  trends are largest in magnitude in the 1990s (Fig. 5(a, d, g, j, m)); however, by the 2010s, these regions of the ocean also exhibit increasing  $C^*$  trends (Fig. 5(c, f, i, l, o)). Similar decreasing  $C^*$  trends ( $\Delta \bar{C}^* <$ 0) in the tropical and equatorial Atlantic (e.g., 1994–1998 for  $\gamma > 27 \text{ kg/m}^3$  in Fig. 1) point to the influence of lower latitude upper ocean circulation cell (L. D. Talley, 2013). There is also the region between 1 and 2 km depth in the Atlantic with  $\Delta C^* < 0$  in the 1990s for the AMOC density layers noted in Fig. 1 and corresponding  $\Delta C^* < 0$  along the upwelling isopycnals in the Southern Ocean.

By the last decade of the analysis period (2003 – 2022), we find  $\widetilde{\Delta C^*}$  to be predominantly positive in all basins and at all depths. The largest rate of increase is within the upper ocean (500–1000 m) and within the deep water formation and sinking of North

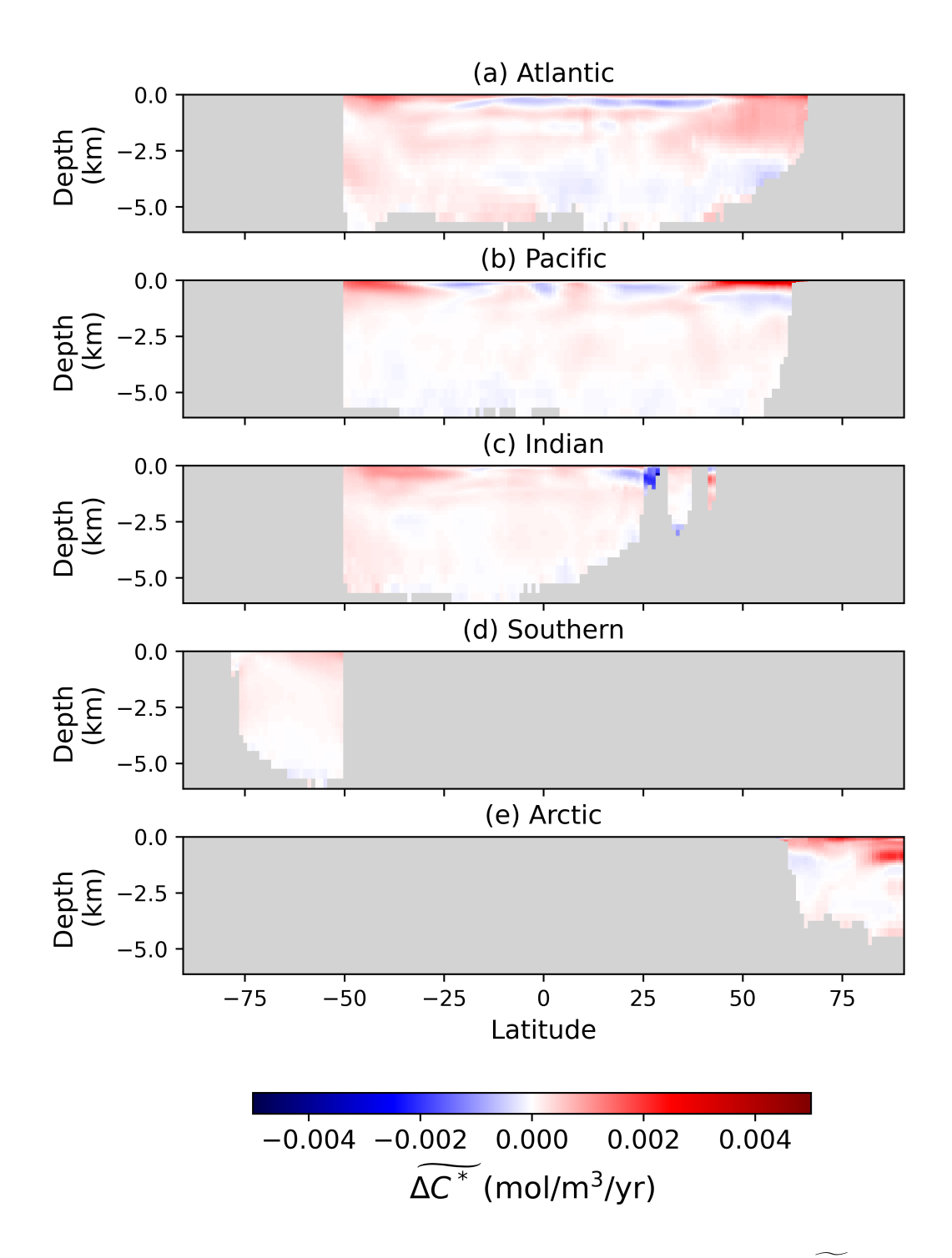
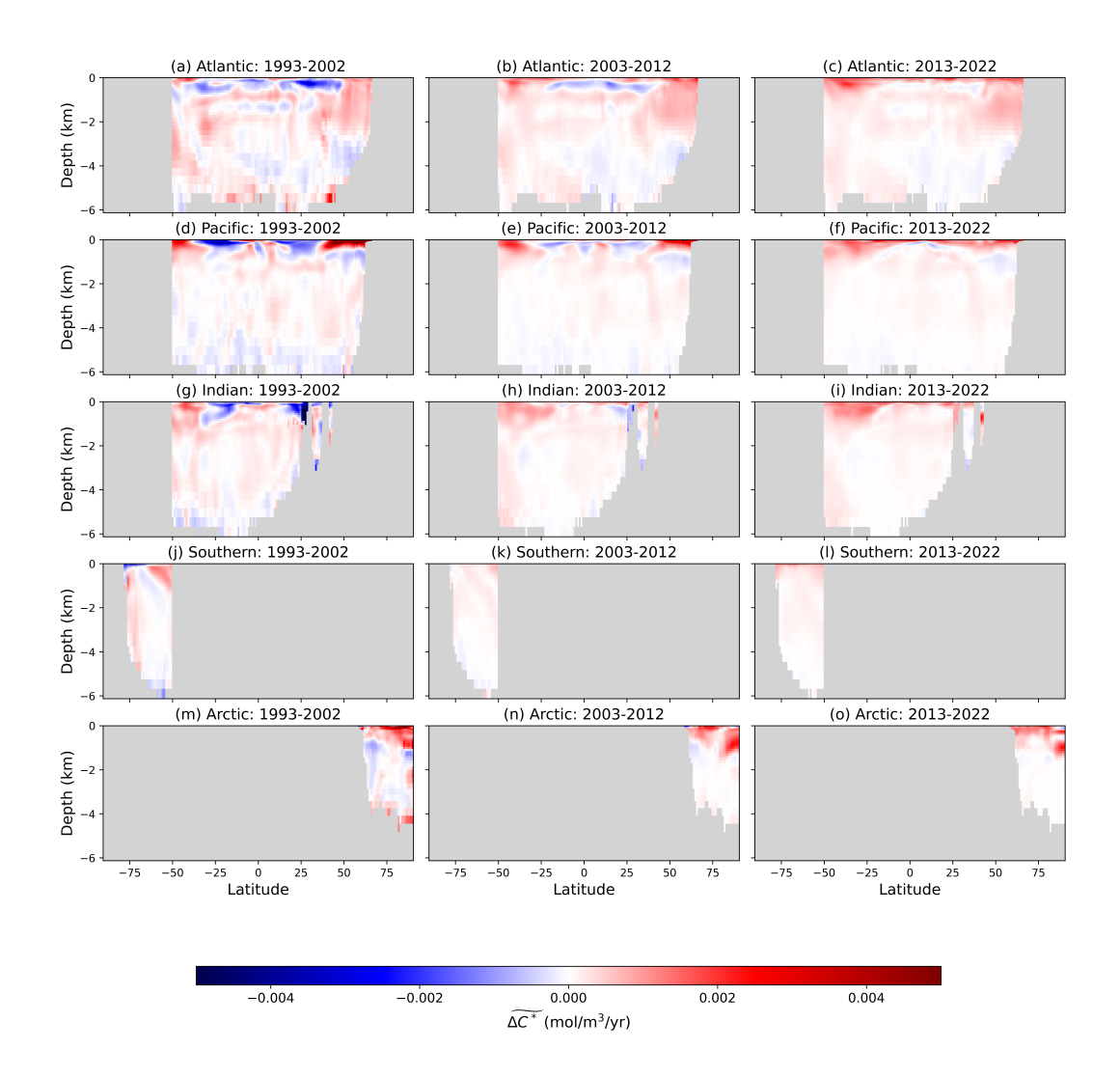
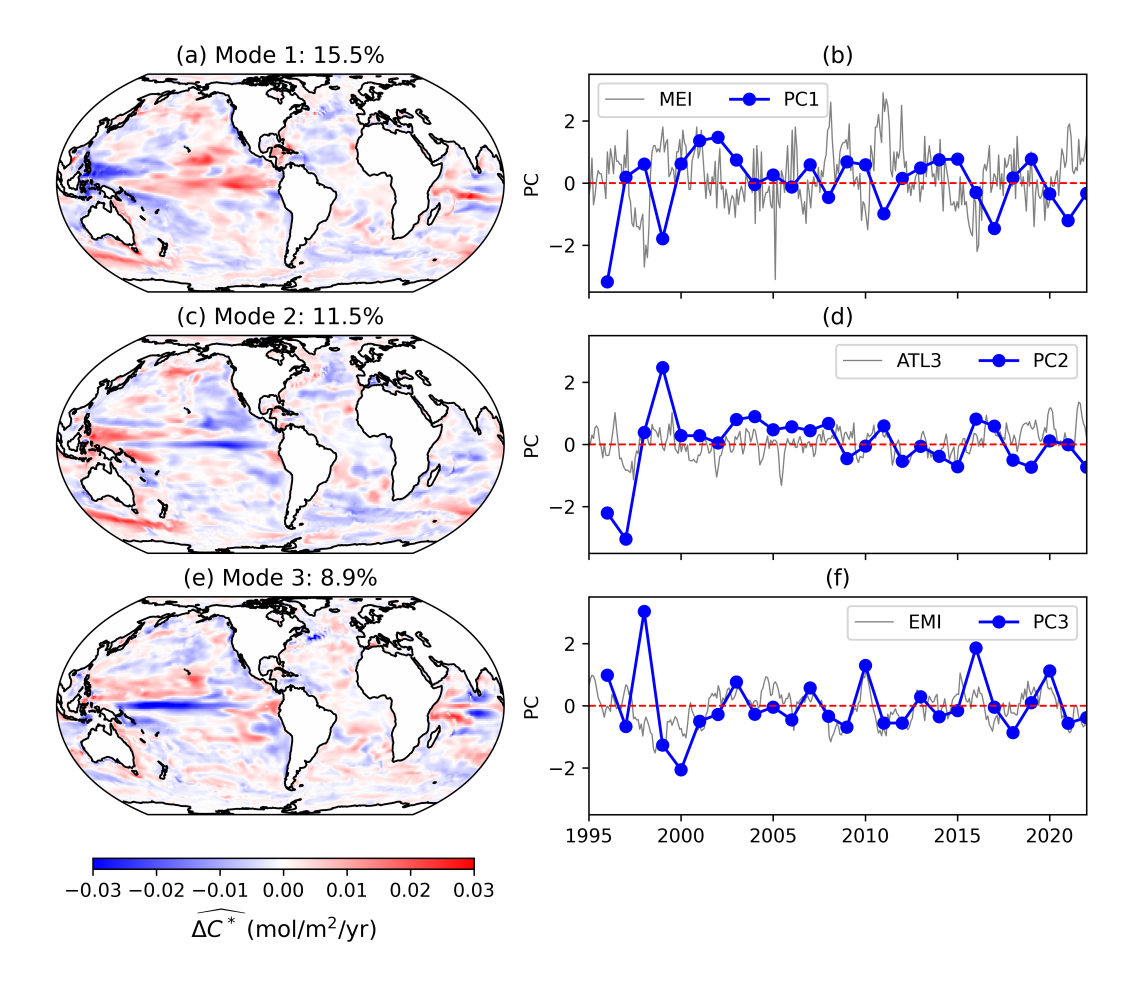


Figure 4. Zonally-averaged trends of ocean anthropogenic carbon concentrations  $(\widetilde{\Delta C^*})$  from 1992 to 2022 in five basins: (a) Atlantic, (b) Pacific, (c) Indian, (d) Southern, and (e) Arctic. Positive (negative) values indicate an increasing (decreasing) anthropogenic carbon concentrations at that latitude-depth position. Land is shaded in grey.



**Figure 5.** Same as Figure 4 but broken down into decadal trends: (a-e) 1993 - 2002, (f-j) 2003-2012, (k-o) 2013-2022.



**Figure 6.** (a, c, e) EOFs and (b, d, f) PC timeseries for the first three modes for  $\widehat{\Delta C^*}$  variability. Indices for the best fitting climate modes are also plotted: (b) Multivariate ENSO Index (MEI), (d) Atlantic 3 Index (ATL3), (f) El Niño Modoki Index (EMI).

Atlantic Deep Water. In particular, large positive  $\widetilde{\Delta C}^*$  trends are found in the upwelling regions of the subtropical South Pacific and Indian Oceans (Fig. 5(i, f)). This is consistent with relatively larger positive trends in the upper ocean and negligible change in ocean anthropogenic DIC reported by Keppler et al. (2023) and Müller et al. (2023). This result also points to ocean anthropogenic carbon predominantly being confined to the upper ocean circulation cell where it can more easily exchange with the atmosphere rather than being stored in the lower circulation cell with longer residence times.

# 3.3 EOF analysis of Interannual Variability of $\Delta C^*$

The annual temporal resolution of our data allows us to examine patterns of interannual variability in further detail. Specifically, we conduct the Empirical Orthogonal Functions (EOF) analysis of the annual maps of vertically-integrated  $\Delta C^*$ . This analysis allows us to identify spatial (EOFs) and temporal (Principal Component (PC) timeseries) patterns that drive interannual variability in  $\Delta C^*$  and compare them to the known climatological modes. Spatial patterns are compared to the global modes of sea surface temperature variability (Messié & Chavez, 2011) that have been shown to align well with climate indices. The analysis is performed using xeof package for Python (Rieger & Levang, 2024). As larger rates of change of  $C^*$  are found within the top 1500 m (Figs. 4, 5), the

analysis is focused on  $\Delta C^*$  vertically integrated over this depth range  $(\widehat{\Delta C^*})$ . The analysis is also limited to the 1995–2022 period to exclude any influence from potential ECCO-Darwin spin-up bias (1992 – 1994).

The first three modes for the variability of  $\widehat{\Delta C^*}$ , which capture about 36% of interannual variability, are shown in Figure 6. Because the distribution of carbon in the ocean is not only governed by circulation (Carroll et al., 2022) and there are most likely lags in the response of carbon distribution to changes in circulation due to climatological modes, the EOFs and PC timeseries are not exactly aligned with the known climatological modes and indices and show patterns of a combination of several climatological modes. Nonetheless, based on the dominant spatial features and comparison of PC timeseries with monthly climate index timeseries, we can approximately attribute these  $\widehat{\Delta C^*}$  modes to the known climate modes.

The first mode EOF resembles the ENSO mode (Fig. 6(a)) and PC1 timeseries roughly aligns with the Multivariate ENSO Index (MEI) (NOAA Physical Sciences Laboratory, 2025) with a lag of about one year (Fig. 6(b)). The second mode is more difficult to attribute to a particular climate mode based on the EOF spatial structure (Fig. 6(c)), but after plotting the PC2 timeseries against different climate indices (e.g., Pacific Decadal Oscillation, North Pacific Gyre Oscillation, Atlantic Multidecadal Oscillation), it is best aligned with the Atlantic 3 Index (ATL3) (NOAA Climate Prediction Center, 2025), in particular after 2010 (Fig. 6(d)). ATL3 captures the variability of Atlantic Niño mode, which is an equatorial and tropical phenomenon in the Atlantic that resembles the Pacific ENSO pattern (Ruiz-Barradas et al., 2000). Finally, the third mode closely resembles the El Niño Modoki mode (Fig. 6(e, f)), with the PC3 timeseries quite closely aligning with the El Niño Modoki Index (EMI) (JAMSTEC, 2025). El Niño Modoki has been indentified as the variability in the equatorial Pacific that is similar to but different from, and sometimes opposite of, the conventional ENSO patterns (Ashok et al., 2007). Overall, this analysis reveals that over a third of the interannual variability in the rate of change  $\Delta C^*$  in the top 1500 m is primarily driven by equatorial and tropical climatological modes.

# 3.4 Total $C^*$ Change

480

481

482

483

484

485

489

490

491

492

493

494

495

496

497

500

501

502

504

505

507

509

510

511

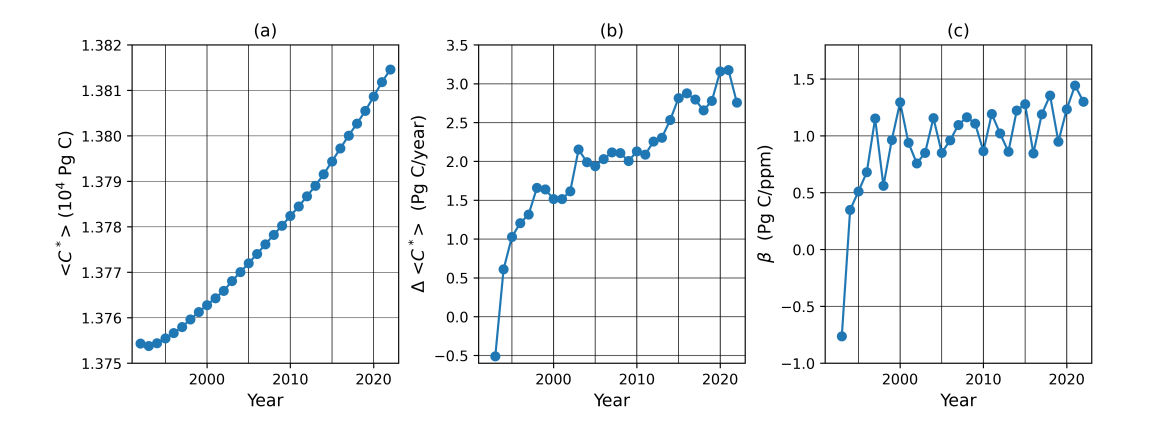


Figure 7. (a) Annual globally-integrated anthropogenic carbon concentration ( $\langle C^* \rangle$ ) from 1992 to 2022, (b) annual rate of change of  $\langle C^* \rangle$ , (c) ratio of  $\langle C^* \rangle$  to global annual mean atmospheric CO<sub>2</sub> concentrations.

Now that we have examined the spatial distribution of the rates of change of ocean anthropogenic DIC concentrations, we provide estimates in  $\Delta C^*$  integrated over the entire ocean. We compare our results with several previous estimates: (1) 51 ± 11 Pg C

change of DIC in the ocean from 2004 to 2019 based on a machine-learning model interpolation of observational data (Keppler et al., 2023), (2) 44–49 Pg C change in anthropogenic ocean carbon based on interpolated observational data over 2004 – 2019 (Gruber et al., 2019; Keppler et al., 2023), and (3) 64 Pg C change in total ocean DIC over the 1995–2017 time period based on ECCO-Darwin model output (Carroll et al., 2022) that we also use in this study.

Figure 7(a) shows  $C^*$  integrated over the entire global ocean (denoted as  $\langle C^* \rangle$ ) from 1992 to 2022. Estimated from Friedlingstein et al. (2022), the total anthropogenic emissions from 1992 to 2022 is approximately 216 PgC, so the portion of the ocean absorption of anthropogenic carbon is around 28%. This value is within the range of  $31\pm7\%$ found by Keppler et al. (2023) over the 2004-2019 time period. Over the 2004-2019 period, the ECCO-Darwin estimate of the increase in anthropogenic carbon storage  $(C^*)$ is 36 Pg C, which is smaller than the total DIC change of 51±11 Pg C reported by Keppler et al. (2023) and closer to the anthropogenic portion (44–49 Pg C  $\pm 6$  Pg C) inferred from the  $C^*$  estimates of Gruber et al. (2019). For 1995 - 2017, the output of the ECCO-Darwin model estimates an anthropogenic  $\langle C^* \rangle$  increase of 45 Pg C, which is smaller than the total DIC change of 64 Pg C reported by Carroll et al. (2022), but consistent with the expectation that  $C^*$  represents only the anthropogenic portion of the total DIC. The total amount of ocean carbon of anthropogenic origin (integrated  $C^*$ ) is about 37% of the total DIC pool estimated by Carroll et al. (2022). However,  $\Delta \langle C^* \rangle$  is approximately 70% of the total DIC change, suggesting that a significant portion of the ocean carbon budget imbalance is influenced by the uptake of anthropogenic emissions.

The linear rate of increase in  $\langle C^* \rangle$  calculated over the entire 1992 – 2022 period is about 1.9 Pg C yr<sup>-1</sup>, which is lower than the  $3.2\pm0.7$  Pg C yr<sup>-1</sup> rate estimated by Keppler et al. (2023). However, consistent with Carroll et al. (2022), who found that the global DIC tendency is increasing over 1995 to 2019, our total  $C^*$  trend (Figure 7(b)) also exhibits an accelerating trend rather than a constant linear increase. This implies that the rate of oceanic anthropogenic carbon uptake  $(d\langle C^*\rangle/dt)$  is not constant. This result reflects the combined effects of increased atmospheric  $CO_2$  concentrations and some potential changes in ocean circulation and ventilation. It should be noted that there could also be some residual model spin-up bias in the early part of the timeseries (1992–1994) (Carroll et al., 2022), so these earlier results, e.g.  $d\langle C^* \rangle/dt < 0$ , should be interpreted with caution. To account for atmospheric change, we also compute  $\beta$ , which is the ratio of  $\langle C^* \rangle$  to the annually-averaged atmospheric CO<sub>2</sub> concentrations (Lan et al., 2025) (Figure 7(c)). During most of our analysis period, we find  $\beta$  to fluctuate over the 0.5– 1.5 Pg C/ppm range with noticeable interannual variability, possibly due to many longterm ocean and atmospheric circulatory patterns. This further suggests the need for a more careful investigation of ocean DIC at finer temporal resolution (seasonal/annual) rather than decadal averages that may not align with any particular circulation cycles.

## 4 Discussion and Conclusions

512

513

516

517

518

521

522

523

525

529

530

531

532

533

534

535

537

538

541

542

543

544

545

548

549

550

551

553

554

555

556

557

561

562

In this study, we present an assessment of interannual and decadal changes in anthropogenic carbon storage in the global ocean from 1992 to 2022, using physically and biogeochemically consistent modeled data from the ECCO-Darwin ocean state estimate (Carroll et al., 2020). The ECCO-Darwin assimilates biogeochemical observations and has shown to have good agreement with GLODAP observational data for DIC (Carroll et al., 2022) making it a good candidate for this analysis. We estimate the portion of ocean DIC attributable to the ocean's uptake of anthropogenic  $CO_2$  from the atmosphere using the quasi-steady tracer  $C^*$  used in previous studies (Clement & Gruber, 2018; Gruber et al., 2019; Müller et al., 2023). However, compared to these prior studies (Gruber et al., 2019; Müller et al., 2023), our approach offers two key extensions. One is that our analysis spans over three decades, with one more recent decade from 2012 to 2022. The other is that because of the higher temporal resolution of the ECCO-Darwin model data,

we are able to examine the interannual variability in the changes in  $C^*$  and more accurately estimate decadal trends using linear regression rather than aggregating data over a decade and computing decadal differences.

Over the full 1992–2022 period, we estimate a total global ocean  $C^*$  increase of approximately 60 Pg C, corresponding to about 28% of total anthropogenic CO<sub>2</sub> emissions during this time, which is consistent with previous estimates over the 2004–2019 time period (Keppler et al., 2023) . The general trend of temporal changes in  $C^*$  shows a nonlinear increase both exhibiting interannual variability and accelerating trend. In the last decade of our analysis (2012–2022), the rate of  $C^*$  increase is within the range of 3.2± 0.7 Pg C/year previously estimated based on observational data (Keppler et al., 2023), but in earlier decades, the rate is below 2 Pg C/year.

To account for the exponentially rising atmospheric CO<sub>2</sub> concentrations, we compute the ratio  $\beta$  of the rate of change of globally-integrated  $C^*$  to the rate of change of atmospheric CO<sub>2</sub> concentration. Over 1995–2022, our analysis shows this ratio to be increasing increasing at a rate of  $\Delta\beta=0.015$  Pg C/ppm/year, indicating that the ocean accumulation of anthropogenic DIC is increasing at faster rate than atmospheric CO<sub>2</sub> accumulation. This estimate differs from the findings of Müller et al. (2023) of  $\Delta\beta<0$ , which suggests a slowdown in the ocean DIC uptake. While the ECCO-Darwin model output has its own biases that could be affecting our estimates, interpolation of observational data such as the method used in Müller et al. (2023) can introduced biases due to spatio-temporal gaps in observations that are skewed towards certain regions and seasons, which tend to be more prevalent in earlier times (e.g., the 1990s). Ultimately, the goal of this study is to add to the existing literature another data point of the estimates of the rates of change of ocean anthropogenic carbon concentrations based on a different dataset such that the overall uncertainty range can be better constrained.

Based on our analysis, the horizontal (depth-integrated,  $\widehat{\Delta C}^*$ ) and vertical (zonallyintegrated,  $\Delta C^*$ ) perspectives taken together reveal a coherent picture of where and how anthropogenic carbon storage has evolved over the past three decades. Across most basins, the large positive  $\Delta \bar{C}^*$  rates are found in near-surface which is upper 1000 m, particularly in 2002–2022, suggesting the incorporation of anthropogenic CO<sub>2</sub> into the mode and intermediate waters in the Pacific and Indian Oceans (L. D. Talley, 2013). Many parts of the ocean exhibit accelerating increasing rates of anthropogenic carbon concentrations, especially over the 2002-2022 period. However, we find that ocean anthropogenic carbon accumulation has been slowing down in certain parts of the ocean, specifically the North and Equatorial Pacific and many parts of Southern Ocean. These correspond to the high-nutrient low-chlorophyll parts of the ocean (Martin et al., 1990; Coale et al., 1996; Parekh et al., 2005) and regions where air-sea CO<sub>2</sub> flux has been identified to drive ocean carbon budget (Carroll et al., 2022). This finding potentially suggests carbon saturation in these parts of the ocean, possibly due to limited downward transport of oceanic carbon as a result of intensified upper-ocean stratification (Sallée et al., 2021; Cheng et al., 2025).

Another important contribution from this study is the EOF analysis of the interannual variability of the rates of change of  $C^*$ , which is possible due to the high and regular temporal resolution of the ECCO-Darwin output compared to observational data. While the EOF modes of  $\widehat{\Delta C^*}$  variability are not expected to completely agree with climate modes unlike the sea surface temperature that more rapidly responds to changes in the sea surface conditions, we find that over a third of the variability can be attributed to equatorial and tropical climate modes, namely ENSO, Atlantic Niño, and El Niño Modoki. While ENSO variability has been noted in previous studies (e.g., Keppler et al., 2020; Carroll et al., 2022), the contribution from the other two climate modes has not been considered as thoroughly. It is also interesting to note that regions with larger values of acceleration or deceleration of  $\widehat{\Delta C^*}$  rates (Fig. 3) are predominantly are outside of the equatorial and tropical regions, i.e., mostly within the subtropical gyres and higher lat-

itudes (the Southern and Arctic Oceans). This suggests that different mechanisms contribute to longer term trends and interannual variability of the rate of change of  $C^*$ .

617

618

619

620

621

622

623

626

627

628

629

630

631

632

633

634

635

638

639

640

641

642

643

646

647

648

649

650

651

It is possible that the timeseries considered here is not long enough to detect climate oscillations with longer periods, such as the Atlantic Multidecadal Oscillation (AMO) (Kerr, 2000). However, we do find the decrease in the North Atlantic uptake of anthropogenic carbon compensated by large increasing rates of  $C^*$  in the near-surface Southern Ocean in the 1990s, reminiscent of the AMO mode spatial pattern. We do not find such compensation in the 2000s and 2010s, possibly corresponding to the shift in AMO index from negative to positive around 2000, whether AMO is due to an internal climate variability or tied to volcanic eruptions such as Mt. Pinatubo in 1991 (Mann et al., 2021). Overall, this analysis points to the need for longer and higher temporal resolution timeseries of  $C^*$  to examine the effects of these internal climate drivers as they might be partially embedded in the computed decadal rates of change, particularly in low- or midlatitude regions.

While this study provides a basin-scale, decadal assessment of anthropogenic carbon trends using a physically consistent and spatially complete ECCO-Darwin model product, several limitations should be acknowledged. First, the use of annual-mean data restricts the resolution of seasonal and short-term variability (Keppler et al., 2020). Second, our specific methodology to separate the natural and anthropogenic carbon concentrations following previous works (Gruber et al., 2019; Müller et al., 2023) uses fixed stoichiometric ratios (e.g., C:P and C:N) for calculation. This may introduce regional biases, especially in areas where C:P deviates from the global Redfield average (Deutsch & Weber, 2012; Martiny et al., 2013; Liefer et al., 2024; Seelen et al., 2025) and omits possible effects of temporal changes in these stoichiometric ratios over such a long timeseries (Hutchins & Tagliabue, 2024; Liu et al., 2025). Third, while the ECCO-Darwin model helps mitigate data sparsity in under-observed regions such as the Arctic, it does not replace direct observations. The absence of high-frequency (e.g., monthly or daily) data limits our ability to resolve fine-scale dynamics and may underestimate short-term variability that affects ocean carbon concentrations (Mahadevan et al., 2004). Finally, because the ECCO-Darwin model output is deterministic, our regression approach does not incorporate uncertainty quantification, which limits the statistical interpretation of differences across time periods or basins. Ultimately, with these limitations in mind, some of which can be addressed in future studies if higher resolution model outputs become available, this study provides an in-depth analysis of the ocean anthropogenic carbon spatiotemporal variability over the past three decades to enhance our understanding of changes in ocean ability to uptake additional CO<sub>2</sub> from the atmosphere.

## Open Research Section

Data for computed  $C^*$  values for each year, analyzed and processed data, and analysis codes are available in the Github repository (https://github.com/bzemskova/anthropogenic\_DIC/) with DOI: 10.5281/zenodo.17633809

ECCO-Darwin model output is available at the ECCO Data Portal: http://data.nas.nasa.gov/ecco.

Global atmospheric carbon dioxide concentrations are available from Lan et al. (2025) through NOAA Global Monitoring Laboratory: https://gml.noaa.gov/ccgg/trends/global.html.

#### Acknowledgments

This research has been supported by the Natural Sciences and Engineering Research Council of Canada (grant numbers: RGPIN-2025-02281 and DGECR-2025-00478) and compute allocation from the Digital Research Alliance of Canada (RRG number 5443).

#### References

- Anderson, L. A., & Sarmiento, J. L. (1994). Redfield ratios of remineralization determined by nutrient data analysis. *Global biogeochemical cycles*, 8(1), 65–80.
- Ashok, K., Behera, S. K., Rao, S. A., Weng, H., & Yamagata, T. (2007). El niño modoki and its possible teleconnection. *Journal of Geophysical Research:* Oceans, 112(C11).
- Bronselaer, B., Russell, J. L., Winton, M., Williams, N. L., Key, R. M., Dunne, J. P., ... Sarmiento, J. L. (2020). Importance of wind and meltwater for observed chemical and physical changes in the southern ocean. *Nature Geoscience*, 13(1), 35–42.
- Broullón, D., Pérez, F. F., Velo Lanchas, A., Hoppema, M., Olsen, A., Takahashi, T., ... Kozyr, A. (2020). A global monthly climatology of oceanic total dissolved inorganic carbon: A neural network approach. *Earth System Science Data Discussions*, 2020, 1–30.
- Bushinsky, S. M., Landschützer, P., Rödenbeck, C., Gray, A. R., Baker, D., Mazloff, M. R., . . . Sarmiento, J. L. (2019). Reassessing southern ocean air-sea co2 flux estimates with the addition of biogeochemical float observations. *Global biogeochemical cycles*, 33(11), 1370–1388.
- Carroll, D., Menemenlis, D., Adkins, J. F., Bowman, K. W., Brix, H., Dutkiewicz, S., ... Zhang, H. (2020). The ecco-darwin data-assimilative global ocean biogeochemistry model: Estimates of seasonal to multidecadal surface ocean pco and air—sea co flux. *Journal of Advances in Modeling Earth Systems*, 12(12), e2019MS001888. doi: 10.1029/2019MS001888
- Carroll, D., Menemenlis, D., Dutkiewicz, S., Lauderdale, J. M., Adkins, J. F., Bowman, K. W., . . . others (2022). Attribution of space-time variability in global-ocean dissolved inorganic carbon. *Global Biogeochemical Cycles*, 36(3), e2021GB007162. doi: 10.1029/2021GB007162
- Carter, B. R., Feely, R. A., Wanninkhof, R., Kouketsu, S., Sonnerup, R. E., Pardo, P. C., . . . others (2019). Pacific anthropogenic carbon between 1991 and 2017. Global Biogeochemical Cycles, 33(5), 597–617.
- Cheng, L., Li, G., Long, S.-M., Li, Y., von Schuckmann, K., Trenberth, K. E., ... others (2025). Ocean stratification in a warming climate. *Nature Reviews Earth & Environment*, 1–19.
- Chin-Yee, S. (2019). Climate Change and Human Security: Case Studies Linking Vulnerable Populations to Increased Security Risks in the Face of the Global Climate Challenge (Strategy Paper). King's College London, EUCERS.

Retrieved from https://discovery.ucl.ac.uk/id/eprint/10084936/7/ Chin-Yee\_Climatechangeandhumansecurity\_VoR.pdf (Version of record hosted on UCL Discovery)

- Clement, D., & Gruber, N. (2018). The emlr( $c^*$ ) method to determine decadal changes in the global ocean storage of anthropogenic co. Global Biogeochemical Cycles, 32(4), 654-679. doi: 10.1002/2017GB005819
- Coale, K. H., Johnson, K. S., Fitzwater, S. E., Gordon, R. M., Tanner, S., Chavez, F. P., . . . others (1996). A massive phytoplankton bloom induced by an ecosystem-scale iron fertilization experiment in the equatorial pacific ocean.

  Nature, 383 (6600), 495–501.
- Deutsch, C., & Weber, T. (2012). Nutrient ratios as a tracer and driver of ocean biogeochemistry. Annual review of marine science, 4(1), 113–141.
- DeVries, T. (2022). The ocean carbon sink. Annual Review of Environment and Resources, 46, 201–230. doi: 10.1146/annurev-environ-120920-111307
- DeVries, T., Holzer, M., & Primeau, F. (2019). Decadal trends in the ocean carbon sink. *Proceedings of the National Academy of Sciences*, 116(24), 11646–11651. doi: 10.1073/pnas.1900371116
- DeVries, T., Yamamoto, K., Wanninkhof, R., Gruber, N., Hauck, J., Müller, J. D., ... Doney, S. C. (2023). Magnitude, trends, and variability of the global ocean carbon sink from 1985 to 2018. *Global Biogeochemical Cycles*, 37(10), e2023GB007780. doi: 10.1029/2023GB007780
- Fay, A., & McKinley, G. (2013). Global trends in surface ocean pco2 from in situ data. Global Biogeochemical Cycles, 27(2), 541–557.
- Friedlingstein, P., O'Sullivan, M., Jones, M. W., Andrew, R. M., Gregor, L., Hauck, J., ... Zheng, B. (2022). Global carbon budget 2022. Earth System Science Data, 14(11), 4811–4900. Retrieved from https://essd.copernicus.org/articles/14/4811/2022/doi: 10.5194/essd-14-4811-2022
- Gray, A. R. (2024). The four-dimensional carbon cycle of the southern ocean. Annual Review of Marine Science, 16, 163-190. doi: 10.1146/annurev-marine -041923-104057
- Gregor, L., & Gruber, N. (2020). Oceansoda-ethz: a global gridded data set of the surface ocean carbonate system for seasonal to decadal studies of ocean acidification. *Earth System Science Data Discussions*, 2020, 1–42.
- Gruber, N., Clement, D., Carter, B. R., Feely, R. A., van Heuven, S., Hoppema, M., ... Wanninkhof, R. (2019). The oceanic sink for anthropogenic co<sub>2</sub> from 1994 to 2007. *Science*, 363 (6432), 1193–1199. doi: 10.1126/science.aau5153
- Gruber, N., & Sarmiento, J. L. (2002). Large-scale biogeochemical-physical interactions in elemental cycles. The sea, 12, 337–399.
- Gruber, N., Sarmiento, J. L., & Stocker, T. F. (1996). An improved method for detecting anthropogenic co<sub>2</sub> in the oceans. Global Biogeochemical Cycles, 10(4), 809–837. doi: 10.1029/96GB01608
- Hutchins, D. A., & Tagliabue, A. (2024). Feedbacks between phytoplankton and nutrient cycles in a warming ocean. *Nature Geoscience*, 17(6), 495–502.
- IPCC. (2023). Sections. in: Climate change 2023: Synthesis report. contribution of working groups i, ii and iii to the sixth assessment report of the intergovernmental panel on climate change. Geneva, Switzerland: IPCC. (Available at: https://www.ipcc.ch/report/ar6/syr/) doi: 10.59327/IPCC/AR6-9789291691647
- Jackett, D. R., & McDougall, T. J. (1997). A neutral density variable for the world's oceans. *Journal of Physical Oceanography*, 27(2), 237–263.
- JAMSTEC. (2025). El nino modoki. https://www.jamstec.go.jp/aplinfo/sintexf/e/elnmodoki/data.html. (Accessed: 2025-11-04)
- Keppler, L., Landschützer, P., Gruber, N., Lauvset, S. K., & Stemmler, I. (2020). Seasonal carbon dynamics in the near-global ocean. Global Biogeochemical Cycles, 34 (12), e2020GB006571.

- Keppler, L., Landschützer, P., Lauvset, S. K., & Gruber, N. (2023). Recent trends and variability in the oceanic storage of dissolved inorganic carbon. *Global Biogeochemical Cycles*, 37(5), e2022GB007677.
  - Kerr, R. A. (2000). A north atlantic climate pacemaker for the centuries. *Science*, 288 (5473), 1984–1985.

- Lan, X., Tans, P., & Thoning, K. (2025). Trends in globally-averaged co2 determined from noaa global monitoring laboratory measurements. doi: 10.15138/9N0H-ZH07
- Landschützer, P., Gruber, N., Haumann, F. A., Rödenbeck, C., Bakker, D. C. E., Van Heuven, S., . . . Wanninkhof, R. (2015). The reinvigoration of the southern ocean carbon sink. Science, 349 (6253), 1221–1224. doi: 10.1126/science.aab2620
- Lauvset, S. K., Lange, N., Tanhua, T., Bittig, H. C., Olsen, A., Kozyr, A., ... others (2022). Glodapv2. 2022: the latest version of the global interior ocean biogeochemical data product. *Earth System Science Data*, 14(12), 5543–5572.
- Liefer, J. D., White, A. E., Finkel, Z. V., Irwin, A. J., Dugenne, M., Inomura, K., ... others (2024). Latitudinal patterns in ocean c: N: P reflect phytoplankton acclimation and macromolecular composition. *Proceedings of the National Academy of Sciences*, 121(46), e2404460121.
- Liu, J., Wang, H., Mou, J., Penuelas, J., Delgado-Baquerizo, M., Martiny, A. C., ... others (2025). Global-scale shifts in marine ecological stoichiometry over the past 50 years. *Nature Geoscience*, 1–10.
- Locarnini, R. A., Mishonov, A. V., Baranova, O. K., Reagan, J. R., Seidov, D., Zweng, M. M., . . . Dukhovskoy, D. (2023). World ocean atlas 2023, volume 1: Temperature. NOAA National Centers for Environmental Information. Retrieved from https://www.ncei.noaa.gov/access/world-ocean-atlas-2023/ (Accessed: 2025-08-13) doi: 10.25923/54bh-1613
- Luetz, J. M., & Merson, J. (2020). Climate change and human migration as adaptation: Conceptual and practical challenges and opportunities. In W. Leal Filho, A. M. Azul, L. Brandli, P. Gökcin Özuyar, & T. Wall (Eds.), Climate action (pp. 120–132). Cham, Switzerland: Springer International Publishing. (Published online 2019; chapter in Encyclopedia of the UN SDGs) doi: 10.1007/978-3-319-95885-9\_46
- Mahadevan, A., Lévy, M., & Mémery, L. (2004). Mesoscale variability of sea surface pco2: What does it respond to? Global Biogeochemical Cycles, 18(1).
- Mann, M. E., Steinman, B. A., Brouillette, D. J., & Miller, S. K. (2021). Multidecadal climate oscillations during the past millennium driven by volcanic forcing. *Science*, 371 (6533), 1014–1019.
- Martin, J. H., Fitzwater, S. E., & Gordon, R. M. (1990). Iron deficiency limits phytoplankton growth in antarctic waters. *Global Biogeochemical Cycles*, 4(1), 5–12.
- Martiny, A. C., Pham, C. T., Primeau, F. W., Vrugt, J. A., Moore, J. K., Levin, S. A., & Lomas, M. W. (2013). Strong latitudinal patterns in the elemental ratios of marine plankton and organic matter. *Nature Geoscience*, 6(4), 279–283.
- Mayot, N., Buitenhuis, E. T., Wright, R. M., Hauck, J., Bakker, D. C. E., & Quéré, C. L. (2024). Constraining the trend in the ocean co<sub>2</sub> sink during 2000–2022. Nature Communications, 15(1), 8429. Retrieved from https://www.nature.com/articles/s41467-024-52641-7 doi: 10.1038/s41467-024-52641-7
- McDougall, T. J., & Barker, P. M. (2017). Getting started with teos-10 and the gibbs seawater (gsw) oceanographic toolbox. SCOR/IAPSO WG, 127, 1-28. Retrieved from https://teos-10.github.io/GSW-Python/density.html
- Messié, M., & Chavez, F. (2011). Global modes of sea surface temperature variability in relation to regional climate indices. *Journal of Climate*, 24 (16), 4314–

4331.

812

813

815

816

817

818

819

821

822

823

824

828

829

830

831

833

834

835

836

837

839

840

841

842

843

846

847

848

849

851 852

853

855

856

857

858

- Müller, J. D., Gruber, N., Carter, B., Feely, R., Ishii, M., Lange, N., . . . Zhu, D. (2023). Decadal trends in the oceanic storage of anthropogenic carbon from 1994 to 2014. *AGU Advances*, 4(4), e2023AV000875. doi: 10.1029/2023AV000875
- NOAA Climate Prediction Center. (2025). Atlantic 3 index (atl3) by month. https://www.cpc.ncep.noaa.gov/products/international/ocean\_monitoring/IODMI/ATL3\_month.html. (Accessed: 2025-11-04)
- NOAA Physical Sciences Laboratory. (2025). Multivariate enso index version 2 (mei.v2). https://www.psl.noaa.gov/enso/mei/. (Accessed: 2025-11-04)
- Parekh, P., Follows, M. J., & Boyle, E. A. (2005). Decoupling of iron and phosphate in the global ocean. *Global Biogeochemical Cycles*, 19(2).
- Pérez, F. F., Mercier, H., Vázquez-Rodríguez, M., Lherminier, P., Velo, A., Pardo, P. C., ... Ríos, A. F. (2013). Atlantic ocean co uptake reduced by weakening of the meridional overturning circulation. *Nature Geoscience*, 6, 146–152. doi: 10.1038/ngeo1680
- Rieger, N., & Levang, S. J. (2024). xeofs: Comprehensive eof analysis in python with xarray. *Journal of Open Source Software*, 9(93). Retrieved from https://doi.org/10.21105/joss.06060 doi: 10.21105/joss.06060
- Rödenbeck, C., Bakker, D. C., Gruber, N., Iida, Y., Jacobson, A. R., Jones, S., ... others (2015). Data-based estimates of the ocean carbon sink variability–first results of the surface ocean pco 2 mapping intercomparison (socom). *Biogeosciences*, 12(23), 7251–7278.
- Rödenbeck, C., DeVries, T., Hauck, J., Le Quéré, C., & Keeling, R. (2021). Databased estimates of interannual sea–air co 2 flux variations 1957–2020 and their relation to environmental drivers. *Biogeosciences Discussions*, 2021, 1–43.
- Ruiz-Barradas, A., Carton, J. A., & Nigam, S. (2000). Structure of interannual-to-decadal climate variability in the tropical atlantic sector. *Journal of Climate*, 13(18), 3285–3297.
- Sabine, C., Key, R., Johnson, K., Millero, F., Poisson, A., Sarmiento, J. L., ... Winn, C. (1999). Anthropogenic co2 inventory of the indian ocean. Global Biogeochemical Cycles, 13(1), 179–198.
- Sallée, J.-B., Pellichero, V., Akhoudas, C., Pauthenet, E., Vignes, L., Schmidtko, S., ... Kuusela, M. (2021). Summertime increases in upper-ocean stratification and mixed-layer depth. *Nature*, 591(7851), 592–598.
- Sarmiento, J., & Gruber, N. (2006). Carbon cycle, co2, and climate; the anthropogenic perturbation. Ocean biogeochemical dynamics, 399–417.
- Seelen, E. A., Gleich, S. J., Kumler, W., Anderson, H. S., Bian, X., Björkman, K. M., . . . others (2025). Nitrogen and phosphorus differentially control marine biomass production and stoichiometry. Nature Communications, 16(1), 5713.
- Talley, L., Feely, R., Sloyan, B., Wanninkhof, R., Baringer, M., Bullister, J., ... others (2016). Changes in ocean heat, carbon content, and ventilation: a review of the first decade of go-ship global repeat hydrography. *Annual review of marine science*, 8, 185–215.
- Talley, L. D. (2013). Closure of the global overturning circulation through the indian, pacific, and southern oceans: Schematics and transports. *Oceanography*, 26(1), 80–97.
- Trebilco, R., Fleming, A., Hobday, A. J., Melbourne-Thomas, J., McDonald,
  J., McCormack, P. C., ... Pecl, G. T. (2022). Warming world, changing ocean: mitigation and adaptation to support resilient marine systems.

  Reviews in Fish Biology and Fisheries, 32(1), 39–63. Retrieved from https://doi.org/10.1007/s11160-021-09678-4 (Published online 21 September 2021; issue date March 2022) doi: 10.1007/s11160-021-09678-4
  - United Nations Development Programme (UNDP). (2023). Mapping of Climate

Change Threats in Arab States: Climate Change, Environmental Degradation and Security Impacts (Technical Report). United Nations Development Programme. Retrieved from https://www.undp.org/sites/g/files/zskgke326/files/migration/arabstates/Mapping-of-Climate-Change-Threats.pdf (PDF accessed via UNDP website)

- Verdy, A., & Mazloff, M. R. (2017). A data assimilating model for estimating s outhern o cean biogeochemistry. *Journal of Geophysical Research: Oceans*, 122(9), 6968–6988.
- Wanninkhof, R., Doney, S. C., Bullister, J. L., Levine, N. M., Warner, M., & Gruber, N. (2010). Detecting anthropogenic co2 changes in the interior atlantic ocean between 1989 and 2005. *Journal of Geophysical Research: Oceans*, 115 (C11).
- Zemskova, V. E., He, T.-L., Wan, Z., & Grisouard, N. (2022). A deep-learning estimate of the decadal trends in the southern ocean carbon storage. *Nature Communications*, 13, 4056. doi: 10.1038/s41467-022-31560-5